Journal of Materials Chemistry A

Reversible Perovskite-Fluorite Phase Transition in Alumina-Supported CeFeOx Films

Journal:	*Journal of Materials Chemistry A*
Manuscript ID	TA-ART-08-2022-006215.R1
Article Type:	Paper
Date Submitted by the Author:	06-Dec-2022
Complete List of Authors:	Shen, Kai; University of Pennsylvania, Chemical and Biomolecular Engineering Fan, Mengjie; University of Pennsylvania, Chemical and Biomolecular Engineering Kwon, Ohhun ; University of Pennsylvania, Chemical and Biomolecular Engineering Viescas, Arthur; Villanova University College of Liberal Arts and Sciences Papaefthymiou, Georgia; Villanova University, Physics; Villanova University Gorte, Raymond; University of Pennsylvania, Chemical and Biomolecular Engineering Vohs, John; University of Pennsylvania, Chemical and Biomolecular Engineering

Reversible Perovskite-Fluorite Phase Transition in Alumina-Supported $CeFeO_x$ Films

Kai Shen,[1] Mengjie Fan,[1] Ohhun Kwon,[1] Arthur J. Viescas,[2] Georgia C. Papaefthymiou,[2] Raymond J. Gorte,[1] and John M. Vohs[1*]

[1] Department of Chemical and Biomolecular Engineering
University of Pennsylvania,
Philadelphia, PA 19104, USA

[2] Department of Physics
Villanova University,
Villanova, PA 19085, USA

*Corresponding Author email: vohs@seas.upenn.edu

Abstract

Thin films with a stoichiometry of $CeFeO_x$ were conformally deposited on high-surface-area γ-Al_2O_3 by Atomic Layer Deposition (ALD). X-ray diffraction (XRD) patterns, High-Resolution Transmission Electron Microscopy (HRTEM) images, Raman spectra, and Mössbauer spectra demonstrated that 2-nm-thick films exhibited a perovskite structure after reduction at 1073 K but converted to a fluorite phase upon oxidation at 1073 K. The transition between the fluorite and perovskite structures was reversible for at least five oxidation and reduction cycles. Coulometric titration at 1073 K showed that reduction of the fluorite phase occurred in two steps, one at a $P(O_2)$ of 10^{-15} atm and a second at a $P(O_2)$ of 10^{-8} atm. X-ray Photoelectron Spectra (XPS) demonstrated that Ce has +3 valence in the perovskite phase and +4 valence in the fluorite phase, while Fe is mixed +2 and +3 valence in the reduced perovskite phase and +3 valence in the fluorite phase. The $CeFeO_x$ thin films were found to retain high surface area and remain conformal to the γ-Al_2O_3 support upon redox cycling suggesting that they may be useful in applications ranging from catalysis to spintronics.

Keywords: Perovskite, Fluorite, $CeFeO_3$, synthesis, thin film, phase transition

1. Introduction

Ceria-based oxides in which a portion of the Ce^{4+} cations in the fluorite lattice have been substituted with a second +4 or +3 metal cation have a range of interesting properties. For example, substituting Zr^{4+} into the CeO_2 produces a mixed ceria-zirconia, $Ce_xZr_{1-x}O_2$, which has enhanced reducibility compared to pure ceria;[1, 2] and this material is widely used in catalytic applications, particularly for oxygen storage in automotive emissions-control systems.[3, 4] Substitution of a small amount of +3 metal cations in the CeO_2 fluorite lattice requires the creation of oxygen ion vacancies for charge compensation. This has been exploited in Gd- and Sm-doped ceria where the induced oxygen vacancies result in high oxygen-ion conductivity at elevated temperatures. These materials can be used as electrolytes in high-temperature electrochemical devices, such as fuel cells.[5]

Recently, there has been interest in iron-doped ceria or mixed oxides of iron and cerium for use as oxygen carriers for chemical looping (CL) processes, including CL methane steam reforming and CL water splitting.[6, 7] Several studies have shown that modifying the CeO_2 with Fe enhances both reducibility and catalytic activity[8-11] and indicate that $CeFeO_3$ may be formed under reducing conditions. Cerium-orthoferrite, $CeFeO_{3-x}$, has a perovskite lattice with a mixed +2/+3 valency for the Fe cations. Due to its multiferroic character, this mixed oxide also has interesting magnetic and electronic properties.[12-14] For example, based on Density Functional Theory (DFT) calculations, Abbad *et al.* have predicted that $CeFeO_3$ is a half-metallic ferromagnet making it of interest for spintronic devices,[14] such as nonvolatile magnetic random-access memories and magnetic sensors,[15] just to name a few. Jabbarzare *et al.* have also reported that nano-powders of $CeFeO_3$ have a light absorption onset at 688 nm, which is in the visible range, suggesting that cerium-orthoferrite may be an active visible-light-driven photocatalyst.[12, 16]

Since +4 is the most stable oxidation state for cerium in the bulk oxide, $Ce^{+3}FeO_3$ is not easily formed, especially under oxidizing conditions.[17, 18] This is in contrast to other rare earth ferrites, such as the perovskites $LaFeO_3$ and $PrFeO_3$, where +3 is the most stable oxidation state for the rare earth cation.[19-21] While synthesis of single-phase, bulk $CeFeO_3$ has proven to be difficult, several methods for its synthesis have been reported in the literature, including solid-state reaction between CeO_2 and Fe_2O_3 at elevated temperatures,[12, 22] microwave processing of cerium and iron nitrate solutions,[23] impregnation of the cerium and iron nitrate solution on a zeolitic imidazolate framework followed by vacuum drying,[24] and sol-gel formation followed by calcination at high temperature.[25] While such approaches are useful for obtaining samples for characterization of the bulk properties of $CeFeO_3$, the high temperature calcination steps that are required generally result in a material with a relatively low surface area ($< 1\ m^2g^{-1}$) which would not be particularly useful for many of the applications mentioned above,[6, 26] where thin films or high-surface-area materials would likely be required. Furthermore, bulk $CeFeO_3$ is unstable under oxidizing conditions at high temperature and tends to irreversibly separate into CeO_2 and Fe_2O_3 phases upon oxidation.[27]

To overcome some of the limitations of the bulk-synthesis methods mentioned above and develop a thin film form of $CeFeO_3$ that could be used in catalytic and other applications where high surface areas are required, here we report the use of Atomic Layer Deposition (ALD) to grow $CeFeO_x$ thin films on a high-surface-area γ-Al_2O_3 support. The results of this study show that a 2-nm thick $CeFeO_x$ film can be reversibly cycled between an oxidized Fe-substituted fluorite CeO_2 phase and a partially reduced perovskite $CeFeO_3$ phase.

2. Experimental section

2.1 Sample preparation

The γ-Al_2O_3 support (Strem Chemicals, Inc.) used in this study was pre-treated by calcination in air at 1173 K for 24 h and had a Brunauer–Emmett–Teller (BET) specific surface area of 125 $m^2 \cdot g^{-1}$. To facilitate handling the γ-Al_2O_3 powder was pressed into thin wafers and then ALD was used to deposit iron oxide and cerium dioxide onto the γ-Al_2O_3 support using a home-built, vacuum ALD apparatus that has been described elsewhere.[28] Tetrakis(2,2,6,6-tetramethyl-3,5-heptanedionato)cerium ($Ce(TMHD)_4$, Strem Chemicals, Inc.) and ferrocene ($Fe(Cp)_2$, Sigma-Aldrich, Inc.) were used as the cerium and iron precursors, respectively. Each ALD deposition cycle consisted of initially evacuating the gas from the tube containing the γ-Al_2O_3 support to a pressure of ~ 0.05 torr and then exposing it to a ~5 Torr of the precursor at 523 K for 5 min followed by oxidizing the sample in air at 773 K for ferrocene or at 873 K for $Ce(TMHD)_4$ to remove the ligands on the precursors and form the oxide. The average Fe and Ce deposition rates were determined gravimetrically to be 6.5×10^{13} Fe atoms$\cdot cm^{-2} \cdot cycle^{-1}$ and 3.9×10^{13} Ce atoms$\cdot cm^{-2} \cdot cycle^{-1}$, respectively, which is consistent with what has been reported by others for similar precursors.[29] Additional evidence that film growth was self-limiting comes from the fact that the amount of oxide added in each cycle was similar to what would be expected for a monolayer coverage of each precursor.[30] To obtain a Ce:Fe molar ratio of 1:1, when growing a $CeFeO_x$ film, every three Fe ALD cycles were followed by five Ce ALD cycles. After depositing the films, they were subjected to five redox cycles prior to the characterization studies. The redox cycles consisted of reduction in 10% H_2 in He for 12 hours, followed by oxidation in 10% air in He for 2 hours at 1073 K.

A bulk $CeFeO_3$ sample was also used in some experiments. This sample was prepared via a rapid solid-solution method, where a mixture of CeO_2 powder (Sigma-Aldrich, Inc.), Fe_2O_3 powder (prepared using the method described by Shen et al.[31]) and Fe powder (J. T. Baker

Chemical) was ball-milled for 24 h. The mixture was then put into a quartz tube which was flushed with a 200 mL·min^{-1} He flow and then evacuated. After the evacuation, the tube was sealed and heated up to 1123 K with a ramping rate of 5 K·min^{-1} and then held at 1123 K for 48 h before cooling down to the room temperature.

2.2 Characterization Methods

A home-built BET apparatus was used to obtain N_2 adsorption isotherms at 78 K and measure the specific surface areas of each sample. X-Ray Diffraction (XRD) was performed using a Rigaku MiniFlex diffractometer with a Cu-Kα source (λ = 0.15416 nm). High-resolution transmission electron microscopy (HRTEM), scanning transmission electron microscopy (STEM), and energy dispersive X-ray spectra (EDS) maps were obtained using a JEOL JEM-F200 STEM, operated at 200 kV. For microscopy studies, the powder samples were diluted in ethanol and then deposited onto carbon support films on copper grids (Electron Microscopy Sciences, USA). X-Ray Photoelectron Spectra (XPS) were acquired in an ultrahigh vacuum chamber equipped with a hemispherical electron energy analyzer (Leybold-Heraeus) and an Al-Kα X-ray source (VG Microtech). To facilitate peak fitting, a Shirley-type background was subtracted from each XPS spectrum. Raman spectra were recorded with an Invia Renishaw microspectrometer equipped with He–Ne 532 nm laser. Raman measurements were carried out with a laser power of 1 mW at the sample and an exposure time of 240 s. Transmission ^{57}Fe Mössbauer spectroscopy measurements were conducted at room temperature using a conventional constant acceleration transducer and a ^{57}Co radioactive source in a Rh matrix. The spectrometer was calibrated using a 6 μm iron foil enriched in ^{57}Fe and all isomer shifts reported are relative to α-Fe at room temperature. The obtained spectra were fitted to a superposition of iron sites using the WMOSS least-square fit

software package (SEE Co., Edina, MN, USA) for data evaluation and identical recoil-free fractions were assumed for all phases and lattice sites.

The oxygen stoichiometries for the $CeFeO_x$ films were measured as a function of $P(O_2)$ at 1073 K (redox isotherm) using a Coulometric Titration (CT) apparatus that consisted of an yttria-stabilized zirconia (YSZ) tube with Pt electrodes affixed on both its inner and outer surfaces.[32] A schematic diagram of the CT system is displayed in Fig. Sup1. Before the CT measurement, approximately 200 mg of sample was placed in the tube (inner volume of ~ 20 cm^3) and heated to 1073 K at a ramping rate of 1 K/min. The sample was then exposed to a flowing gas stream of 3% H_2O, 10% H_2 and 87% He for 12 h, after which both ends of the tube were sealed. A Gamry Instruments potentiostat was used to apply a voltage between the two Pt electrodes in order to pump oxygen into or out of the cell through the oxygen-ion conducting YSZ tube. The total amount of O_2 transferred was determined by integration of the current over time. The $P(O_2)$ in the closed cell was obtained from the Open-Circuit Voltage (OCV) between two Pt electrodes using the Nernst equation.

The oxygen uptake by reduced samples was also measured by flow titration. For these measurements, 300 mg of the sample were placed in a tubular reactor and heated to 1073 K in dry air. The sample was then exposed to a mixture of 10% H_2 in He at a flowrate of 60 $mL \cdot min^{-1}$ for 12 h. The sample was then re-oxidized by exposing it to a stream of 10% dry air in He at a flowrate of 60 $mL \cdot min^{-1}$. A mass spectrometer (SRS RGA-100) connected to the reactor outlet was used to record the composition of the effluent gas. The amount of O_2 consumed during re-oxidation of the sample was determined by integrating the difference between N_2 and O_2 mass-spectrometer signals.

3. Results

3.1 BET and XRD characterization

The $CeFeO_x$ films were grown on the γ-Al_2O_3 support by ALD to a total weight loading of 61% (~47 % volume fraction of $CeFeO_3$). Assuming the film was uniform over the entire γ-Al_2O_3 surface with the same density as that of bulk $CeFeO_3$, this weight loading corresponds to a nominal thickness of ~2 nm (4-5 unit cells) As shown in Fig. Sup2, the sample mass increased linearly with the number of ALD super-cycles (one super-cycle consists of 3 cycles of Fe and 5 cycles of Ce). We will refer to samples prepared in this way as $CeFeO_x/\gamma$-Al_2O_3. The BET surface area of these samples after five redox cycles at 1073 K was 37 $m^2 \cdot g^{-1}$, which is about one-third of that of the high-temperature annealed γ-Al_2O_3 support. This difference can be attributed mainly to the mass increase from the $CeFeO_3$ film and to a lesser extent a decrease in the average pore diameter due to the thickness of the conformal film.

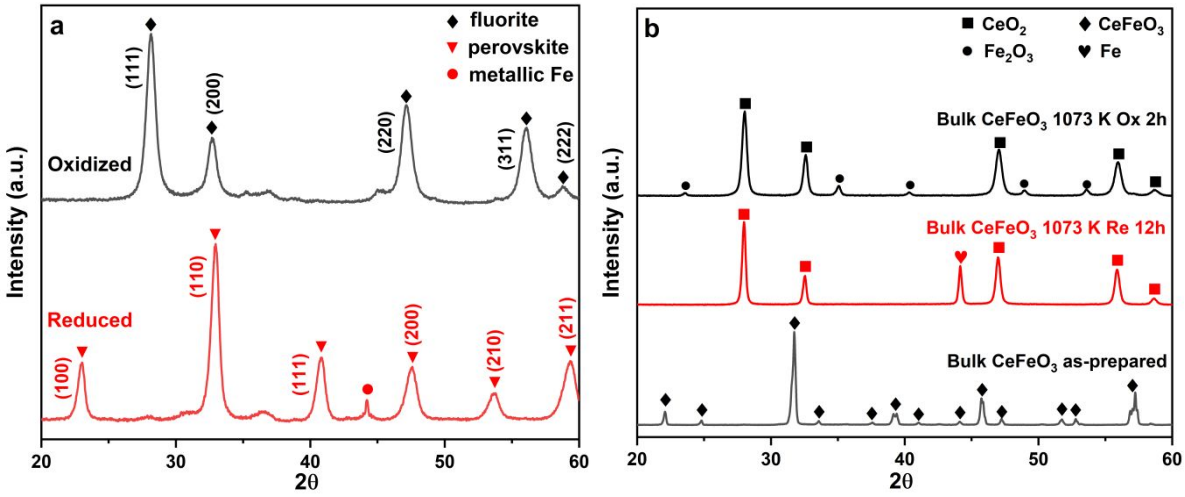

Fig. 1 XRD patterns of (a) $CeFeO_x/\gamma$-Al_2O_3 sample oxidized in dry air at 1073 K and reduced in H_2 at 1073 K and (b) bulk $CeFeO_3$ as-prepared, and after oxidation in dry air at 1073 K and reduced in humidified H_2 at 1073 K.

XRD patterns of oxidized and reduced $CeFeO_x/\gamma\text{-}Al_2O_3$ are shown in Fig. 1a, and those of the as-prepared, oxidized, and reduced bulk-$CeFeO_3$ sample are shown in Fig. 1b. For the thin film $CeFeO_x/\gamma\text{-}Al_2O_3$, the oxidized sample was exposed to a flowing 10% air and 90% He gas stream for 2 hours at 1073 K and then cooled to room temperature in the same gas flow, while the reduced sample was exposed to a flowing 10% H_2 and 90% He gas stream for 12 hours at 1073 K and then cooled to room temperature in the same gas flow. The oxidized bulk $CeFeO_3$ was obtained by calcinating the as-prepared bulk $CeFeO_3$ in a 10% air and 90% He flowing gas stream at 1073 K for 2 h, and the reduced bulk $CeFeO_3$ was obtained by treating the sample in flowing humidified H_2 (3% H_2O, 10% H_2 and 87% He) at same temperature for 12 h.

The XRD pattern of the oxidized-$CeFeO_x/\gamma\text{-}Al_2O_3$ sample contains prominent peaks that are close to those expected for the fluorite lattice of CeO_2 (the peaks are assigned in the figure)[33, 34] with a few additional very small peaks being present between 35 and 46 degrees 2θ. The lattice parameter of the oxidized $CeFeO_x/\gamma\text{-}Al_2O_3$ is estimated to be 0.55 nm from the XRD pattern, which is close to that of cubic CeO_2 (0.541 nm). The slightly higher lattice constant the thin film may be due to some incorporation of some Fe^{3+} into the fluorite phase. The as-prepared bulk $CeFeO_3$ sample exhibits a characteristic perovskite XRD pattern (Fig. 1b) that is consistent with that reported previously for this material.[13, 35] After calcination in air at 1073 K, however, the bulk sample separated into two phases, which can be identified as CeO_2 and $\alpha\text{-}Fe_2O_3$. [36-38] This result is distinct from that of the thin-film sample, where $\alpha\text{-}Fe_2O_3$ peaks were not observed for the oxidized sample.

Upon reduction, the $CeFeO_x/\gamma\text{-}Al_2O_3$ sample undergoes a phase change and the XRD pattern for this sample contains peaks consistent with a cubic perovskite lattice. The estimated lattice

parameter from the XRD pattern is 0.39 nm for the reduced $CeFeO_x/\gamma$-Al_2O_3 sample. While XRD data reported for cubic $CeFeO_3$ is not available in the literature, the lattice parameter for the thin film is close to that of cubic perovskite $LaFeO_3$ which is 0.392 nm. This indicates that the lattice constant for the thin film perovskite is smaller than that of the bulk material. This may result either from interactions with the underlying γ-Al_2O_3 support or differences in the oxygen stoichiometry between the bulk and thin film samples. As will be discussed below, for the reduction conditions used here, the cerium ferrite in the thin film sample has a stoichiometry of $CeFeO_{2.6.}$ For the $CeFeO_x/\gamma$-Al_2O_3 sample, in addition to the perovskite peaks, there is a small peak at 44 degrees 2θ which can be assigned to metallic Fe. A different result was again obtained for the bulk sample where the XRD pattern of the reduced sample is composed of peaks characteristic of fluorite CeO_2 and metallic iron. This result demonstrates that the perovskite phase of the bulk $CeFeO_3$ sample cannot be restored by reduction after being calcined in air at 1073 K and separating into two phases (CeO_2 and α-Fe_2O_3). This is in contrast to the thin film sample where the phase changes that took place upon redox cycling were reversible. As shown by the XRD data in Fig. Sup3, the perovskite phase is stable in air at temperatures up to 873 K where it starts to convert to the fluorite $CeFeO_x$ phase.

3.2 Electron Microscopy

Fig. 2 presents a STEM image of a $CeFeO_x/\gamma$-Al_2O_3 sample that had been subjected to five oxidation and reduction cycles at 1073 K, along with the EDS maps of Ce, Fe and Al for the indicated region. These data show correspondence between the elemental maps of the three elements, which is consistent with the $CeFeO_x$ film being uniform and conformal to the γ-Al_2O_3 support and remaining so upon redox cycling at high temperature.

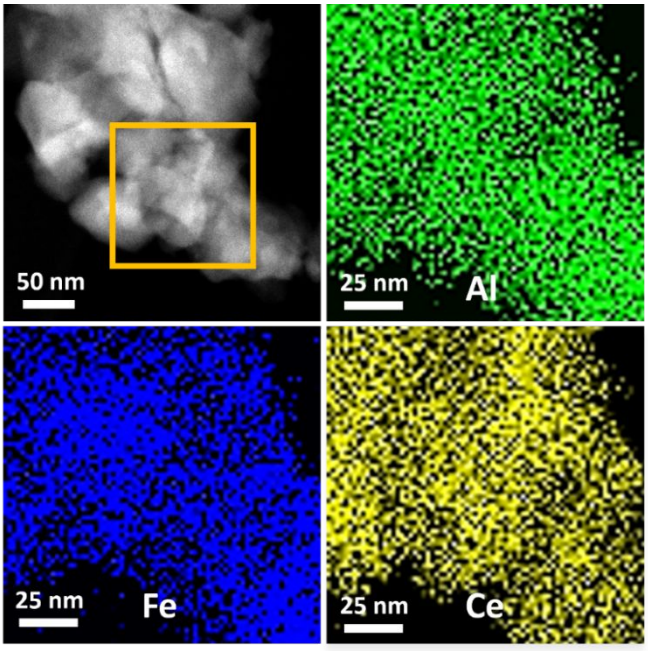

Fig. 2 STEM-EDS of reduced $CeFeO_x/\gamma\text{-}Al_2O_3$. The sample was pretreated by 5 redox cycles followed by reduction in dry hydrogen at 1073K. The STEM image is in the upper left and the elemental EDS maps correspond to the designated area in this image.

To obtain additional insight into the structure of the $\gamma\text{-}Al_2O_3$-supported $CeFeO_x$ films, HRTEM images of the oxidized and the reduced samples were obtained. Fig. 3a shows a HRTEM image of the oxidized-$CeFeO_x/\gamma\text{-}Al_2O_3$. A HRTEM image of the bare $\gamma\text{-}Al_2O_3$ support is shown in Figure Sup5. A Fast-Fourier-Transform (FFT) diffractogram of the indicated area is also included in the figure. The image contains well-defined lattice fringes which are not present with the bare $\gamma\text{-}Al_2O_3$ support, allowing them to be assigned to the $CeFeO_x$ thin film. The FFT pattern shows (111) and (200) planes along [011] zone axis (ZA) orientation, consistent with a fluorite lattice. Fig. 3b and 3c show two separate HRTEM images of reduced $CeFeO_x/\gamma\text{-}Al_2O_3$ and the associated FFT diffraction patterns of the indicated areas. Both images contain well-defined lattice fringes and from the FFT diffractograms (100) and (110) planes consistent with a cubic perovskite lattice can be identified along [001] and [111] ZA orientations, respectively. These results provide further

support for the fluorite to perovskite phase transition upon reduction of the $CeFeO_x/\gamma\text{-}Al_2O_3$ sample.

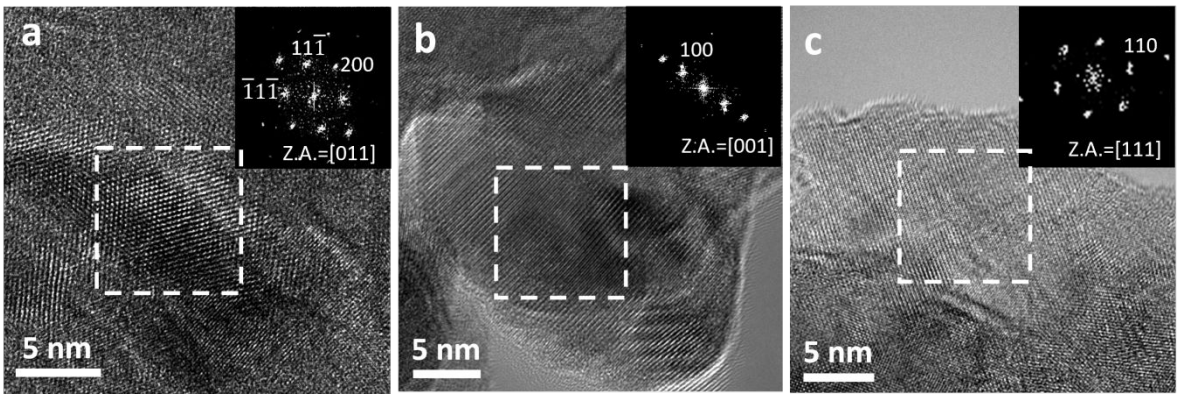

Fig. 3 HRTEM and corresponding FFT diffraction patterns of the indicated areas of (a) oxidized $CeFeO_x/\gamma\text{-}Al_2O_3$; (b) and (c) reduced $CeFeO_x/\gamma\text{-}Al_2O_3$. The samples were pretreated with 5 redox cycles followed by oxidation or reduction in dry air or hydrogen at 1073K to obtain the oxidized or reduced state. The insets correspond to the diffraction pattern obtained from the designated region in each image.

3.3 Phase diagram

The redox isotherm of the $CeFeO_x/\gamma\text{-}Al_2O_3$ sample at 1073 K, measured using CT, is displayed in Fig. 4. For these data, we started with a sample that was reduced in a stream of 3% H_2O, 10% H_2 and 87% He at 1073 K prior to sealing the CT tube. The composition of the sample as a function of $P(O_2)$ was then measured with the $P(O_2)$ being varied by electrochemically pumping O_2 into or out of the CT cell. To calibrate the x value for the $CeFeO_x$ composition scale, we assumed that the fully oxidized $CeFeO_x/\gamma\text{-}Al_2O_3$ sample had an overall stoichiometry of $CeFeO_{3.5}$, (*i.e.*, the sample contained only Ce^{4+} and Fe^{3+}). This calibration was corroborated by consistency between the flow-titration and the CT measurements. Both methods gave an x value close to 2.6 for the reduced sample. Note that the $\gamma\text{-}Al_2O_3$ support is not reducible for the conditions used in these measurements. The redox isotherm in Fig. 4 contains two distinct steps or phase transitions at

$P(O_2)$ values of 10^{-8} atm and 10^{-15} atm. The former corresponds to equilibrium between $CeFeO_{3.5}$ and $CeFeO_3$, and the latter corresponds to equilibrium between $CeFeO_3$ and $CeFeO_{2.6}$.

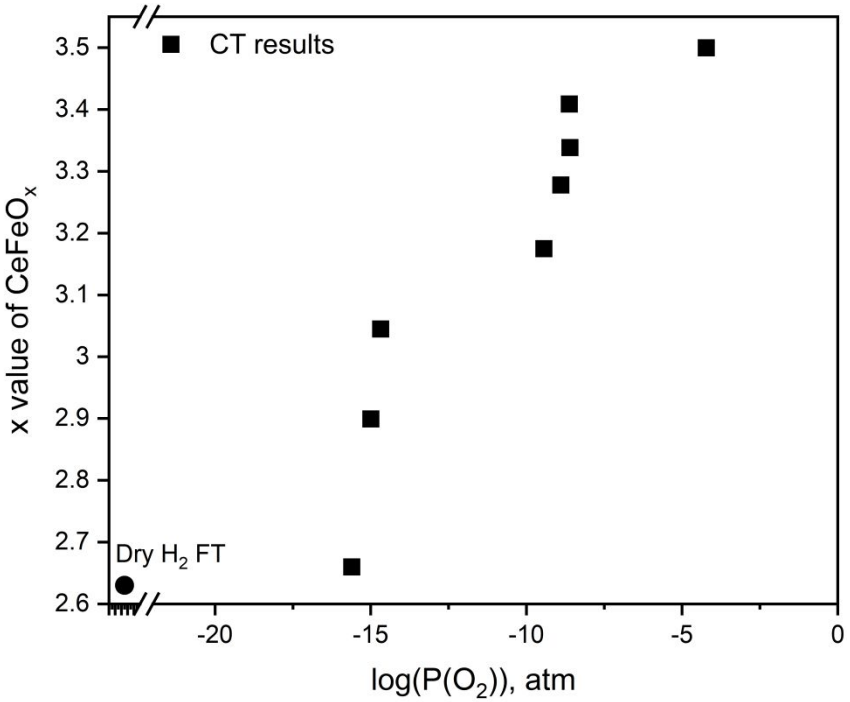

Fig. 4 CT redox isotherm of $CeFeO_x/\gamma\text{-}Al_2O_3$ at 1073 K (solid squares). The sample was pretreated with 5 redox cycles at 1073 K before the measurement. The oxygen stoichiometry of the dry-hydrogen-reduced sample is also shown in the figure (solid circle) and was measured by flow titration (FT).

3.4 XPS characterization

Ce(3d) and Fe(2p) XPS spectra obtained from oxidized and reduced $CeFeO_x/\gamma\text{-}Al_2O_3$ samples are displayed in Fig. 5. Curve resolution of each Ce(3d) spectrum, assuming Gaussian peak shapes, are also included in the figure. Since Fe(2p) photoemission peaks are composed of several overlapping peaks resulting from different multiplet splitting final states[39, 40] it is difficult to use curve fitting to deconvolute different oxidation states in Fe(2p) spectrum. For this reason, we have not included curve fits for these spectra. Fig. 5a shows the Ce($3d_{3/2}$) and Ce($3d_{5/2}$) spectra for a fully oxidized $CeFeO_x/\gamma\text{-}Al_2O_3$ sample (annealed in air at 1073 K for 2h). This spectrum contains

three $3d_{3/2}$ - $3d_{5/2}$ doublets, labeled u/v, u′′/v′′ and u′′′/v′′′, and is consistent with that reported for Ce^{4+}.[41-43] The u′′′/v′′′ peaks centered at 916.9 and 899.0 eV correspond to the primary photoemission from Ce^{4+}, while the u-v and u"-v" doublets are shakedown features resulting from transfer of one or two electrons from the filled O(2p) orbital to an empty Ce(4f) orbital during photoemission.[41, 42] The u′′′ peak is commonly used as a signature for Ce^{4+}, although its concentration does not show a linear dependence on its intensity.[44]

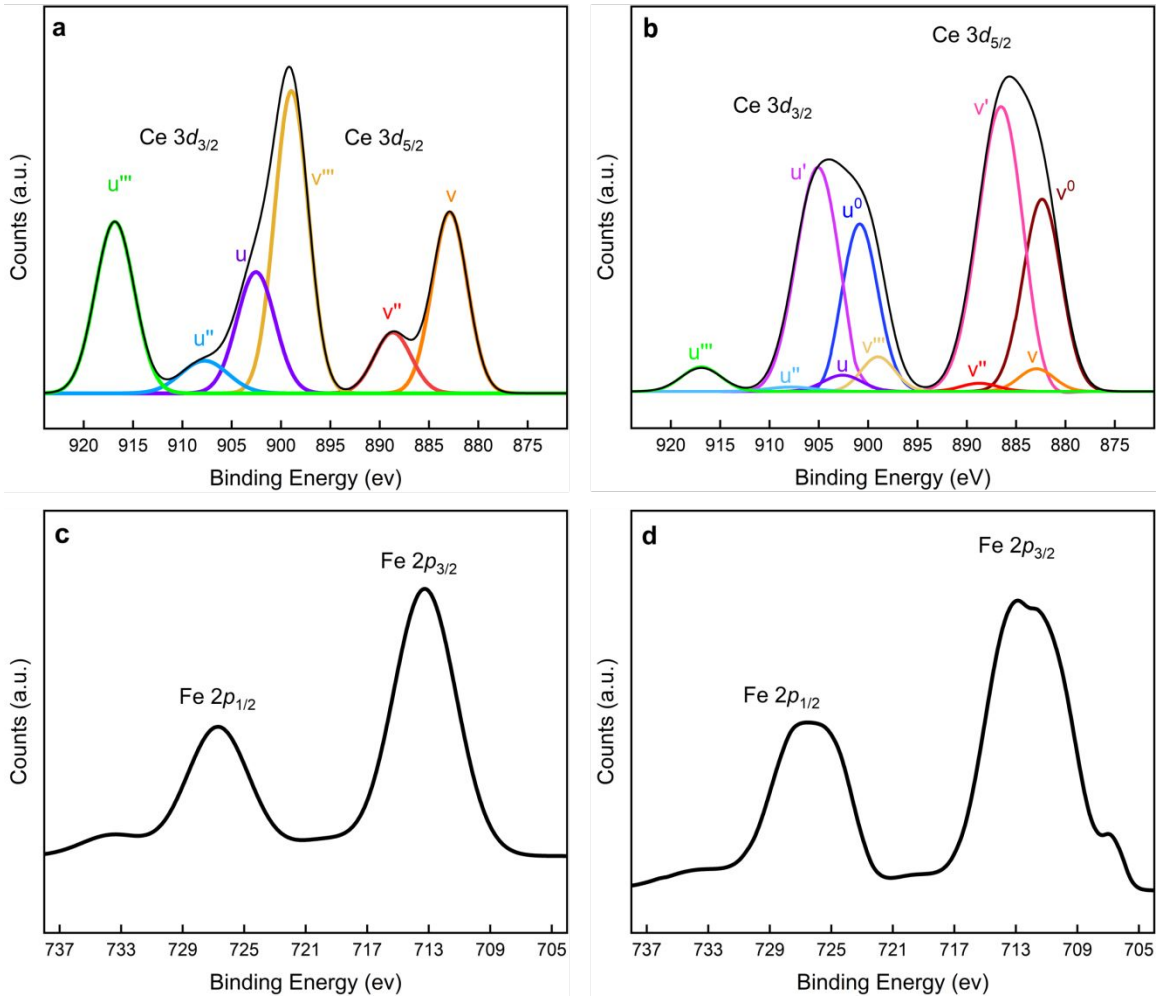

Fig. 5 XPS spectra of the Ce $3d_{3/2}$ and Ce $3d_{5/2}$ regions of (a) oxidized $CeFeO_x/\gamma\text{-}Al_2O_3$ and (b) reduced $CeFeO_x/\gamma\text{-}Al_2O_3$ and XPS spectra of the Fe $2p_{1/2}$ and Fe $2p_{3/2}$ regions of (c) oxidized $CeFeO_x/\gamma\text{-}Al_2O_3$ and (d) reduced $CeFeO_x/\gamma\text{-}Al_2O_3$. The sample was pretreated by 5 redox cycles followed by oxidaiton or reduction in dry air or hydrogen at 1073K to obtain the oxidized or reduced state.

Fig. 5b shows the Ce(3d) spectrum for the $CeFeO_x/\gamma\text{-}Al_2O_3$ sample after reduction in dry H_2 at 1073 K. This spectrum is dominated by two $3d_{3/2}$ - $3d_{5/2}$ doublets, labeled u^0/v^0 and u′/v′, which are characteristic of Ce^{3+}.[41, 44] The u'/v' doublet at 904.9 and 886.4 eV corresponds to the primary photoemission from Ce^{+3}, while the u^o/v^o doublet is a shakedown feature resulting from transfer of one electron from a filled O 2p orbital to a Ce(4f) orbital during photoemission. This spectrum also contains a small u′′′/v′′′ doublet indicating that the sample contains a small amount of Ce^{4+}. Since the reduced sample was exposed to air prior to being loaded into the XPS spectrometer, it is possible that this feature is due to a slight reoxidation of the surface. Taken together, the Ce(3d) XPS spectra demonstrate that the cerium cations are predominantly in the +4-oxidation state in the fully oxidized sample and in the +3-oxidation state in the reduced sample.

Fe(2p) XPS spectra for the oxidized and reduced $CeFeO_x/\gamma\text{-}Al_2O_3$ samples are displayed in Fig. 5c and 5d, respectively. In the spectrum for the oxidized sample, the of Fe($2p_{1/2}$) and Fe($2p_{3/2}$) peaks are centered at 726.8 and 713.2 eV which, along with the accompanying satellite features, are characteristic of Fe^{3+}.[45-47] As shown in Fig. 5d, upon reduction the Fe(2p) peaks become significantly broadened towards lower binding energies which is consistent with reduction of a portion of the Fe^{3+} ions to Fe^{2+}. The shape of this spectrum is also consistent with that reported in the literature for Fe^{3+}/Fe^{2+} mixed valent Fe_3O_4.[47] Unfortunately, due to the aforementioned complexities associated with the multiplet splitting features in Fe(2p) spectra, it is not possible to use these data to obtain a reliable estimate of the Fe^{2+}:Fe^{3+} ratio in this sample. The similarity of the peak shape to that reported for Fe_3O_4 suggests that the ratio is close to 1:2, but this is only a rough estimate. Also note that the spectrum of the reduced sample contains a small peak at 706.3 eV can be assigned to metallic Fe,[48] which is consistent with the XRD data for this sample. A summary of the XPS results has been provided in Table 1.

Table 1. Summary of XPS results

	Peak Positions	
	Oxidized $CeFeO_x/\gamma\text{-}Al_2O_3$	Reduced $CeFeO_x/\gamma\text{-}Al_2O_3$
Ce($3d_{3/2}$)	u''' at 916.9 eV	u' at 904.9 eV
Ce($3d_{5/2}$)	v''' at 899.0 eV	v' at 886.4 eV
Fe($2p_{1/2}$)	726.8 eV	726.1 eV
Fe($2p_{3/2}$)	713.2 eV	712.2 eV
Cation oxidation states	Ce^{4+}, Fe^{3+}	Mainly Ce^{3+}, Fe^{3+}/Fe^{2+} with small amounts of Ce^{4+} and metallic Fe

3.5 Raman spectroscopy

Raman spectra of oxidized (in air at 1073 K) and reduced (in H_2 at 1073 K) $CeFeO_x/\gamma\text{-}Al_2O_3$ samples are shown in Fig. 6. The spectrum of the oxidized sample contains a single prominent band at 462 cm^{-1} corresponding to the triply degenerate F_{2g} mode of the fluorite lattice which consists of a symmetric breathing vibration of the tetrahedrally coordinated O^{2-} anions about the unit cell center.[49] It is noteworthy that this spectrum does not contain any features attributable to

Fe_2O_3, suggesting that the Fe cations are either in an amorphous phase or substituted into the fluorite lattice.

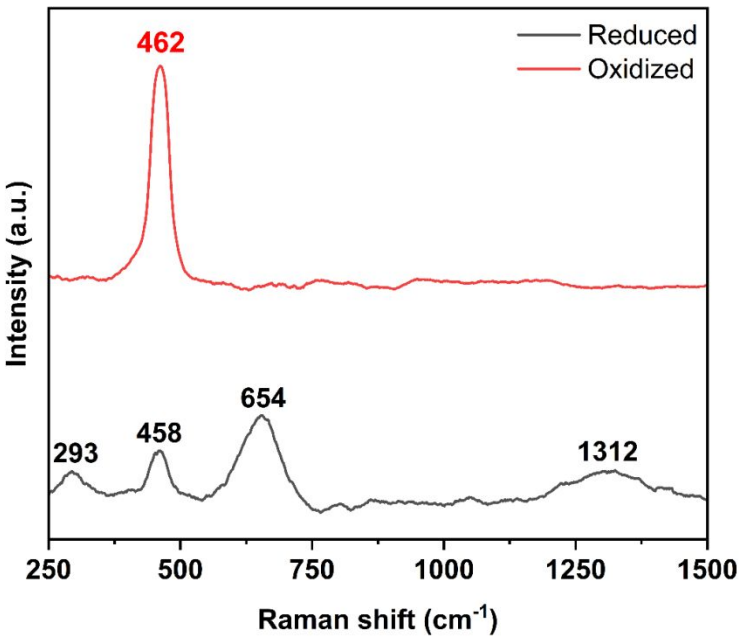

Fig. 6 Raman spectra of the reduced and oxidized $CeFeO_x/\gamma$-Al_2O_3. The sample was pretreated by 5 redox cycling followed by oxidaiton or reduction in dry air or hydrogen at 1073K to obtain the oxidized state or reduced state.

A significantly different spectrum was obtained from the reduced sample which contains peaks at 293 cm^{-1}, 458 cm^{-1}, 654 cm^{-1} and 1312 cm^{-1}. This spectrum is similar to that reported for other rare-earth ferrite perovskites;[50-52] and, by comparison to these previous studies, the bands at 293 cm^{-1} and 458 cm^{-1} can be assigned to A_g modes associated with FeO_6 in-phase rotation and O-Fe-O bending, respectively.[51] The broad peak at 1312 cm^{-1} is generally assigned to two-phonon scattering.[52] There is some disagreement about the assignment of the peak 654 cm^{-1} with various studies assigning it to two phonon scattering,[53] an impurity related feature,[54] or oxygen vacancies.[55] While there may be uncertainty in the peak assignments, the Raman results are consistent with the reduced film, which has a stoichiometry close to $CeFeO_{2.6}$, having a perovskite lattice structure.

3.6 Mössbauer spectroscopy

The ^{57}Fe Mössbauer spectra of the oxidized and the reduced $CeFeO_x/\gamma$-Al_2O_3 samples were recorded to obtain additional information about the valence state and coordination symmetry of Fe cations in these samples. Fig. 7a shows the Mössbauer spectrum of oxidized $CeFeO_x/\gamma$-Al_2O_3 that was calcined in air at 1073 K. The spectrum consists of two superimposed spectral subcomponents: a paramagnetic doublet S1 contributing 80% of the total spectral absorption area, and a magnetic sextet S2 with 20% of the total spectral absorption area. Fitted Mössbauer parameters are given in Table 2. The isomer shift, $\delta = 0.31 \pm 0.03$ mm/s, and quadrupole splitting, $\Delta Eq = 1.00 \pm 0.05$ mm/s, of S1 indicate high spin ferric ions situated at tetrahedral or distorted octahedral coordination lattice sites. The magnetic sextet, with isomer shift $\delta = 0.38 \pm 0.03$ mm/s, quadrupolar shift $\varepsilon = -0.23$ mm/s and magnetic hyperfine field $H_{hf} = 51.35 \pm 0.05$ T of S2, is consistent with antiferromagnetic iron oxide α-Fe_2O_3. Both, S1 and S2 spectra have isomer shifts characteristic of trivalent Fe cations.[56, 57] The magnetic subcomponent indicates the formation of bulk hematite (α-Fe_2O_3) which appears as only a minor component in the XRD pattern of the oxidized sample (the small peaks 35.2, 49.2 and 53.8 degrees 2θ in Fig. 1a).[36, 37]

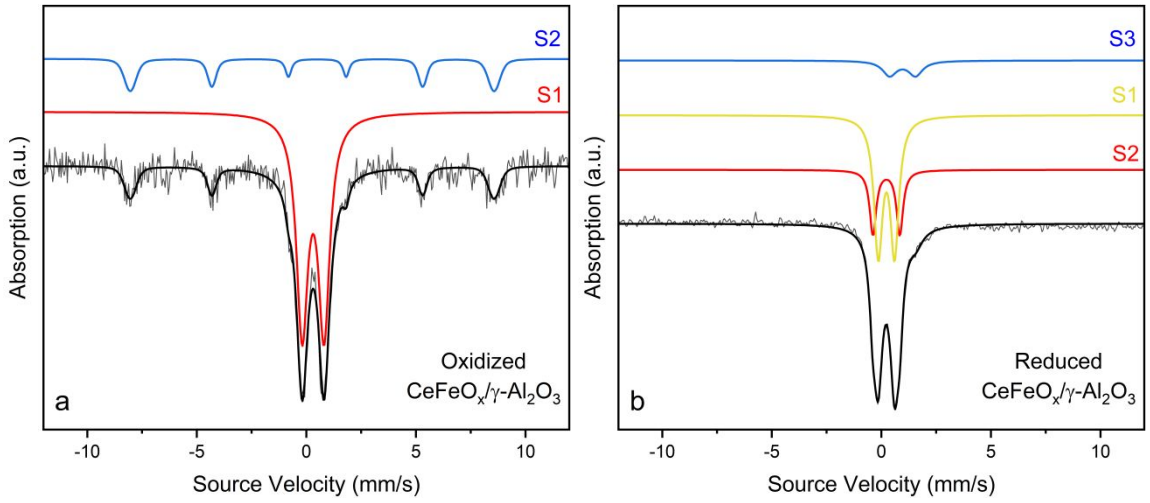

Fig. 7 Mössbauer spectra at 298 K of (a) oxidized and (b) reduced $CeFeO_x/\gamma\text{-}Al_2O_3$. The oxidized sample was calcined in air at 1073 K for 2 h and the reduced sample was pre-treated in 3% humidified H_2 flow at 1073 K for 12 h. Fitted parameters are given in Tables 1 and 2.

Fig. 7b presents the Mössbauer spectrum of the reduced $CeFeO_x/\gamma\text{-}Al_2O_3$ that was pre-treated in wet hydrogen at 1073 K. The overall spectral profile presents an asymmetric, broadened doublet with a small diffuse shoulder around +2 mm/s. The spectrum was best fitted assuming the superposition of three unresolved quadrupolar sites: S1, contributing 65% of spectral absorption area, S2 with 24% of spectral absorption area, and S3 with 11% of spectral absorption area. Fitted Mössbauer parameters are shown in Table 3. The dominant doublet S1 with an isomer shift δ = 0.23 ± 0.03 mm/s and quadrupole splitting ΔE_q = 0.74 ± 0.05 mm/s is indicative of ferric (Fe^{3+}) high-spin ions in an octahedrally coordinated lattice site. Site S2 has a similar isomer shift but a larger quadrupole splitting of ΔE_q = 1.22 ± 0.05 mm/s consistent with high-spin ferric (Fe^{3+}) ions in tetrahedral or highly distorted octahedral symmetry. The third site S3 has an isomer shift δ = 0.97 ± 0.03 mm/s and quadrupole splitting ΔE_q = 1.18 ± 0.05 mm/s characteristic of high-spin ferrous (Fe^{2+}) cations[58] in octahedral symmetry.

Table 2. Isomer shift (*IS*), quadrupole splitting (*QS*) and magnetic hyperfine field (H_{hf}) for the oxidized $CeFeO_x/\gamma\text{-}Al_2O_3$ sample

Site	*IS** (mm/s)	*QS or ε* (mm/s)	H_{hf} (T)	*Area* (%)	Site/Phase Identification
S1	0.31±0.03	1.00±0.05	-	80±5	High-spin ferric (Fe^{3+}) cations in tetrahedral or highly distorted octahedral symmetry
S2	0.38±0.03	-0.23±0.05	51.35±0.05	20±5	$\alpha - Fe_2O_3$

*Isomer shifts are relative to α-Fe.

Table 3. Isomer shift (*IS*) and quadrupole splitting (*QS*) for the reduced $CeFeO_x/\gamma$-Al_2O_3 sample

Site	*IS** (mm/s)	*QS* (mm/s)	*Area* (%)	Site Identification
S1	0.23±0.03	0.74±0.05	65±5	High-spin ferric (Fe^{3+}) cations in octahedral symmetry
S2	0.23±0.03	1.22±0.05	24±5	High-spin ferric (Fe^{3+}) cations in tetrahedral or highly distorted octahedral symmetry
S3	0.97±0.03	1.18±0.05	11±5	High-spin ferrous (Fe^{2+}) cations in octahedral symmetry

*Isomer shifts are relative to α-Fe.

The above results indicate that the reduced sample has a stoichiometry very close to $CeFeO_3$ rather than $CeFeO_{2.6}$ as measured by coulometric titration. Note, however, that the Mössbauer measurements were conducted ex-situ using a quenched reduced sample that was exposed to air at room temperature for several days and this may have resulted in some of the Fe^{2+} cations being oxidized to Fe^{3+} prior to analysis. It is noted that the Mössbauer spectra of the thin-film $CeFeO_3/\gamma$-Al_2O_3 obtained in this study, are mainly composed of paramagnetic high-spin Fe^{3+} unlike those reported for bulk $CeFeO_3$, where only sextets were observed.[59] This may result from the 2-D confinement effect of the thin-film, leading to distorted octahedral sites occupied by high-spin Fe^{3+} cations. The only sextet observed in our samples was in the case of oxidized thin-film of $CeFeO_3/\gamma$-Al_2O_3 (20% of the absorption area) which may be due to bulk hematite (α-Fe_2O_3).

4. Discussion

In this study, we prepared 2-nm-thick, conformal films of a mixed cerium-iron oxide with a nominal 1:1 Ce:Fe cation ratio on a high surface area γ-Al_2O_3 support by ALD. After oxidation at high temperatures, the film exhibited both XRD and TEM diffraction patterns characteristic of a fluorite lattice with the presence of only a small amount of Fe_2O_3 being indicated by XRD. The

Raman spectrum of the oxidized film contained a peak at 462 cm^{-1}, which is close to the characteristic band for bulk fluorite CeO_2 at 465 cm^{-1},[49] and did not contain any bands that could be associated with Fe_2O_3. These results all point to the film having a fluorite structure with the Fe cations being substituted into the CeO_2 lattice. However, the Mössbauer spectra indicate the presence of a minor magnetic component due to bulk hematite, so formation of a small amount of this phase cannot be ruled out.

Since XPS showed that the Fe cations were in the +3-oxidation state, their substitution for Ce^{4+} in the fluorite lattice would require some form of charge compensation. This could be accomplished by reduction of a portion of the Ce^{4+} cations to Ce^{3+} or by the formation of oxygen vacancies. The XPS results for the oxidized sample in Fig. 5 do not provide evidence for the former. The latter would require vacancies on 12.5% of the oxygen lattice sites, which would be expected to give rise to strong features in the Raman spectrum,[57] which were not observed. It is also not clear if the fluorite structure could be maintained for such a high concentration of oxygen vacancies. Another possibility for the required charge compensation is the presence of Fe^{3+} interstitial cations as proposed by Li *et al*.[60] This group also observed low oxygen vacancy concentrations in nanoscale $Ce_{1-x}Fe_xO_2$ solid solutions, which they attributed to the Fe^{3+} cations being distributed on both the fluorite lattice cation sites and interstitial sites in an approximately 3:1 ratio. This conclusion is consistent with characterization data obtained here for the oxidized $CeFeO_{3.5}/\gamma$-Al_2O_3 sample.

The CT data in Fig. 4 show that, at 1073 K, the fully oxidized $CeFeO_{3.5}$ thin film undergoes reduction and a phase change at a $P(O_2)$ of 10^{-8} atm to produce a material that has an overall stoichiometry close to $CeFeO_3$. The Mössbauer spectrum of the $CeFeO_x/\gamma$-Al_2O_3 sample reduced

in humidified-H_2 is consistent with this and indicates that the majority of the Fe cations in this mildly reduced sample are in the +3-oxidation state.

Based on the ΔG of reductions for the binary oxides, Fe_2O_3 and CeO_2, the Fe^{3+} cations would be expected to be more easily reduced than the Ce^{4+} cations.[61] The equilibrium $P(O_2)$ for the Fe_2O_3/Fe_3O_4 phase transition at 1073 K, $10^{-8.5}$ atm is also close to the transition observed here. Based on these observations, one might conclude that the phase transformation involves the reduction of the Fe^{3+} cations in the fluorite mixed oxide to Fe^{2+} to produce perovskite $Ce^{4+}Fe^{2+}O_3$ however, as will be discussed below, the fact that the more highly reduced sample contained a mixture of Fe^{3+} and Fe^{2+} strongly argues against this. The other possibility is that this reduction step involves conversion of Ce^{4+} to Ce^{3+} to produce perovskite $Ce^{3+}Fe^{3+}O_3$. Since reduction of CeO_2 to Ce_2O_3 (*i.e.*, Ce^{4+} to Ce^{3+}) occurs at a $P(O_2)$ of 10^{-20} atm at 1073 K,[62] this would be a surprising result. It is possible, however, that the high stability of the perovskite structure provides a sufficient thermodynamic driving force to induce reduction of the Ce^{4+} to Ce^{3+} in the mixed oxide at the unusually high $P(O_2)$ of 10^{-8} atm. This conclusion is also consistent with a study by Moog *et al.* of the redox properties of Fe-doped CeO_2.[63] In that study, they used XANES to monitor changes in the cation oxidation states in a $Ce_{0.85}Fe_{0.15}O_2$ sample while heating in H_2 and concluded that reduction of Ce^{4+} to Ce^{3+} occurs prior to reduction of Fe^{3+} to Fe^{2+}. Under reducing conditions, Fe can react with Al_2O_3 to form $FeAl_2O_4$;[31] therefore, it is noteworthy that XRD did not provide any evidence for the formation of this compound, which again points to the high stability of the perovskite phase.

The CT data shows that, at 1073 K, the $CeFeO_3$ film undergoes an additional reduction/phase transformation at a $P(O_2)$ of 10^{-15} atm to produce a material with a stoichiometry close to $CeFeO_{2.6}$. A $CeFeO_x/\gamma$-Al_2O_3 sample that was reduced in flowing H_2 at 1073 K also had this stoichiometry

as determined by flow titration. For this highly reduced sample, XRD and TEM showed that the perovskite structure was maintained and XPS showed that the Ce cations were predominantly in the +3 oxidation state, while the Fe cations were a mixture of Fe^{2+} and Fe^{3+}, a result that is consistent with previous studies of cerium orthoferrite.[12, 13] Note that the Fe(2p) XPS data suggest that the Fe^{2+}:Fe^{3+} ratio may be close to 1:2 which is lower than expected for $CeFeO_{2.6}$; but it is possible that the surface layer was partially re-oxidized due to exposure to air prior to XPS analysis. Note that a somewhat different result is obtained from analysis of the Mössbauer spectra. Under the assumption of identical recoil free fractions at all iron lattice sites, the percent spectral absorption areas given in Tables 1 and 2 can be translated into relative abundance of the various sites within the sample. The relative amount of Fe^{2+} thus deduced by Mössbauer spectroscopy in the reduced $CeFeO_x/\gamma$-Al_2O_3 sample predicts a Fe^{2+}:Fe^{3+} ratio of 1:9, much lower compared to the XPS studies. Two effects may contribute to this discrepancy (a) the sample was oxidized over time while Mössbauer data were being collected, and (b) the recoil-free fraction at the ferrous ion lattice site is much smaller than that at the ferric ion sites. The latter would indicate that the Fe^{2+} ion is rather loosely bound to the lattice, pointing to a lower coordination number compared to the Fe^{3+} ions, or being interstitial in nature.

The Ce^{4+}/Ce^{3+} redox couple that is accessible in the $CeFeO_x/\gamma$-Al_2O_3 samples allows for the reversible removal/addition of a significant fraction oxygen from/to the $CeFeO_x$ lattice, a property that could likely be exploited in chemical looping processes. These redox properties, along with the relatively high surface area of the samples, may also allow $CeFeO_x$ thin films to be active catalysts for oxidation reactions and make them attractive as supports for transition-metal oxidation catalysts. These are properties that we plan to explore in future studies. The ease of synthesis of the perovskite $CeFeO_3$ thin films using ALD, relative to bulk synthesis techniques,

may also allow for the multiferroic properties of this interesting material to be more easily exploited.

5. Conclusions

In this study, we have demonstrated the ALD synthesis of conformal thin films of $CeFeO_3$ on a high surface area γ-Al_2O_3 support. Under oxidizing conditions, the films have a fluorite structure and a stoichiometry of $CeFeO_{3.5}$ in which Fe^{3+} cations are substituted into the lattice with additional interstitial Fe^{3+} cations providing charge compensation. At 1073 K and a $P(O_2)$ of 10^{-8} atm, the $CeFeO_{3.5}$ undergoes reduction and a phase transition to $CeFeO_3$ consistent with the formation of a perovskite phase in which both the Ce and Fe cations are in the +3-oxidation state. At a $P(O_2)$ of 10^{-15} atm further reduction occurs to produce perovskite $CeFeO_{2.6}$ which contains Ce^{3+} and a mixture of Fe^{2+} and Fe^{3+}. Redox cycling of this material has demonstrated that these phase transitions are reversible and can take place while preserving the conformal nature of the $CeFeO_x$ thin film.

Author contributions

Kai Shen: Conceptualization, Methodology, Investigation, Writing – original draft. **Mengjie Fan:** Investigation. **Ohhun Kwon:** Investigation. **Arthur J. Viescas:** Investigation. **Georgia C. Papaefthymiou**: Investigation, Writing – original draft. **Raymond G. Gorte:** Supervision, Writing – review & editing. **John M. Vohs:** Supervision, Writing – review & editing.

Conflicts of interest

There are no conflicts of interest to declare.

Acknowledgements

The authors thank the American Chemical Society Petroleum Research Fund for providing support for this research. Some of the work was performed at the Singh Center for Nanotechnology at the University of Pennsylvania, a member of the National Nanotechnology Coordinated Infrastructure (NNCI) network, which is supported by the National Science Foundation (Grant NNCI-1542153).

Supporting Information

The supporting information file provides the schematic diagram of the coulometric titration system, data for the mass increase of $CeFeO_3$ on the γ-Al_2O_3 support, X-ray diffraction (XRD) patterns of reduced $CeFeO_x/\gamma$-Al_2O_3 after being calcined in air at different temperatures for 12 h, XRD patterns of the $CeFeO_x/\gamma$-Al_2O_3 sample reduced in 3% H_2O, 10% H_2, and 87% He at 1073 K for 12 h, the TEM image of bare γ-Al_2O_3 annealed at 1173 K for 24 h, and the TEM image of the $CeFeO_3/\gamma$-Al_2O_3 sample reduced in 10% dry H_2 for 12 h.

References

1. P. R. Shah, T. Kim, G. Zhou, P. Fornasiero and R. J. Gorte, *Chemistry of Materials*, 2006, **18**, 5363-5369.
2. T. Kim, J. M. Vohs and R. J. Gorte, *Industrial & Engineering Chemistry Research*, 2006, **45**, 5561-5565.
3. J. Kaspar, P. Fornasiero and N. Hickey, *Catalysis Today*, 2003, **77**, 419-449.
4. R. Di Monte and J. Kaspar, *Journal of Materials Chemistry*, 2005, **15**, 633-648.
5. T. Montini, M. Melchionna, M. Monai and P. Fornasiero, *Chemical Reviews*, 2016, **116**, 5987-6041.
6. X. Zhu, Y. G. Wei, H. Wang and K. Z. Li, *International Journal of Hydrogen Energy*, 2013, **38**, 4492-4501.
7. X. Zhu, M. Y. Zhang, K. Z. Li, Y. G. Wei, Y. Zheng, J. H. Hu and H. Wang, *Chemical Engineering Science*, 2018, **179**, 92-103.
8. K. Z. Li, M. Haneda, Z. H. Gu, H. Wang and M. Ozawa, *Materials Letters*, 2013, **93**, 129-132.
9. S. W. Ma, S. Y. Chen, A. Soomro, M. Zhu and W. G. Xiang, *International Journal of Hydrogen Energy*, 2018, **43**, 3154-3164.
10. N. C. Means, S. Hammache, W. A. Burgess, B. H. Howard and M. W. Smith, *Energy & Fuels*, 2020, **34**, 871-878.
11. F. R. Garcia-Garcia and I. S. Metcalfe, *Catalysis Communications*, 2021, **160**, 1-6.
12. S. Jabbarzare, M. Abdellahi, H. Ghayour, A. Arpanahi and A. Khandan, *Journal of Alloys and Compounds*, 2017, **694**, 800-807.
13. L. Hou, L. Shi, J. Y. Zhao, S. M. Zhou, S. Y. Pan, X. Y. Yuan and Y. Xin, *Journal of Alloys and Compounds*, 2019, **797**, 363-369.
14. A. Abbad, W. Benstaali, H. A. Bentounes, S. Bentata and Y. Benmalem, *Solid State Communications*, 2016, **228**, 36-42.
15. I. Zutic, J. Fabian and S. Das Sarma, *Reviews of Modern Physics*, 2004, **76**, 323-410.
16. N. S. Arul, D. Mangalaraj, R. Ramachandran, A. N. Grace and J. I. Han, *Journal of Materials Chemistry A*, 2015, **3**, 15248-15258.
17. K. Kitayama, K. Nojiri, T. Sugihara and T. Katsura, *Journal of Solid State Chemistry*, 1985, **56**, 1-11.
18. T. Naganuma and E. Traversa, *Nanoscale*, 2012, **4**, 4950-4953.
19. C. Vazquez-Vazquez, P. Kogerler, M. A. Lopez-Quintela, R. D. Sanchez and J. Rivas, *Journal of Materials Research*, 1998, **13**, 451-456.
20. L. Ma, S. Y. Ma, X. F. Shen, T. T. Wang, X. H. Jiang, Q. Chen, Z. Qiang, H. M. Yang and H. Chen, *Sensors and Actuators B-Chemical*, 2018, **255**, 2546-2554.
21. Z. Q. Zhou, L. Guo, H. X. Yang, Q. Liu and F. Ye, *Journal of Alloys and Compounds*, 2014, **583**, 21-31.
22. M. Robbins, G. K. Wertheim, A. Menth and R. C. Sherwood, *Journal of Physics and Chemistry of Solids*, 1969, **30**, 1823-1825.
23. P. S. Tang, J. J. Zhang, M. B. Fu, F. Cao and C. Y. Lv, *Integrated Ferroelectrics*, 2013, **146**, 99-104.
24. Z. K. Zhang, H. X. Zhang, Y. Hou, P. Z. Liu, X. D. Hao, Y. Z. Liu, B. S. Xu and J. J. Guo, *Journal of Materials Chemistry A*, 2022, **10**, 13013-13020.
25. L. L. Petschnig, G. Fuhrmann, D. Schildhammer, M. Tribus, H. Schottenberger and H. Huppertz, *Ceramics International*, 2016, **42**, 4262-4267.
26. N. L. Galinsky, A. Shafiefarhood, Y. G. Chen, L. Neal and F. X. Li, *Applied Catalysis B-Environmental*, 2015, **164**, 371-379.
27. J. Zou, J. Oladipo, S. L. Fu, A. Al-Rahbi, H. P. Yang, C. F. Wu, N. Cai, P. Williams and H. P. Chen, *Energy Conversion and Management*, 2018, **171**, 241-248.

28. T. M. Onn, S. Y. Zhang, L. Arroyo-Ramirez, Y. Xia, C. Wang, X. Q. Pan, G. W. Graham and R. J. Gorte, *Applied Catalysis B-Environmental*, 2017, **201**, 430-437.
29. R. L. Puurunen, *Journal of Applied Physics*, 2005, **97**, 121301-121352.
30. T. Keuter, G. Mauer, F. Vondahlen, R. Iskandar, N. H. Menzler and R. Vassen, *Surface & Coatings Technology*, 2016, **288**, 211-220.
31. K. Shen, J. M. Paige, O. Kwon, R. J. Gorte and J. M. Vohs, *Industrial & Engineering Chemistry Research*, 2021, **60**, 12228-12234.
32. I. Baldychev, R. J. Gorte and J. M. Vohs, *Journal of Catalysis*, 2010, **269**, 397-403.
33. B. M. Reddy, K. N. Rao, G. K. Reddy, A. Khan and S. E. Park, *Journal of Physical Chemistry C*, 2007, **111**, 18751-18758.
34. M. M. Natile, G. Boccaletti and A. Glisenti, *Chemistry of Materials*, 2005, **17**, 6272-6286.
35. S. J. Yuan, Y. M. Cao, L. Li, T. F. Qi, S. X. Cao, J. C. Zhang, L. E. DeLong and G. Cao, *Journal of Applied Physics*, 2013, **114**, 113909-113912.
36. S. K. Mohapatra, S. E. John, S. Banerjee and M. Misra, *Chemistry of Materials*, 2009, **21**, 3048-3055.
37. A. A. Tahir, K. G. U. Wijayantha, S. Saremi-Yarahmadi, M. Mazhar and V. Mckee, *Chemistry of Materials*, 2009, **21**, 3763-3772.
38. P. Simons, K. P. Torres and J. L. M. Rupp, *Journal of Materials Chemistry A*, 2022, **10**, 8898-8910.
39. A. P. Grosvenor, B. A. Kobe, M. C. Biesinger and N. S. McIntyre, *Surface and Interface Analysis*, 2004, **36**, 1564-1574.
40. M. C. Biesinger, B. P. Payne, A. P. Grosvenor, L. W. M. Lau, A. R. Gerson and R. S. Smart, *Applied Surface Science*, 2011, **257**, 2717-2730.
41. D. A. Creaser, P. G. Harrison, M. A. Morris and B. A. Wolfindale, *Catalysis Letters*, 1994, **23**, 13-24.
42. A. Pfau and K. D. Schierbaum, *Surface Science*, 1994, **321**, 71-80.
43. A. Pfau, K. D. Schierbaum and W. Gopel, *Surface Science*, 1995, **331**, 1479-1485.
44. E. Beche, P. Charvin, D. Perarnau, S. Abanades and G. Flamant, *Surface and Interface Analysis*, 2008, **40**, 264-267.
45. D. Flak, Q. L. Chen, B. S. Mun, Z. Liu, M. Rekas and A. Braun, *Applied Surface Science*, 2018, **455**, 1019-1028.
46. T. Fujii, F. M. F. de Groot, G. A. Sawatzky, F. C. Voogt, T. Hibma and K. Okada, *Physical Review B*, 1999, **59**, 3195-3202.
47. T. Yamashita and P. Hayes, *Applied Surface Science*, 2008, **254**, 2441-2449.
48. B. J. Tan, K. J. Klabunde and P. M. A. Sherwood, *Chemistry of Materials*, 1990, **2**, 186-191.
49. R. Schmitt, A. Nenning, O. Kraynis, R. Korobko, A. I. Frenkel, I. Lubomirsky, S. M. Haile and J. L. M. Rupp, *Chemical Society Reviews*, 2020, **49**, 554-592.
50. M. C. Weber, M. Guennou, H. J. Zhao, J. Iniguez, R. Vilarinho, A. Almeida, J. A. Moreira and J. Kreisel, *Physical Review B*, 2016, **94**, 214103-214108.
51. X. H. Zhang, C. L. Pei, X. Chang, S. Chen, R. Liu, Z. J. Zhao, R. T. Mu and J. L. Gong, *Journal of the American Chemical Society*, 2020, **142**, 11540-11549.
52. M. Popa, J. Frantti and M. Kakihana, *Solid State Ionics*, 2002, **154**, 437-445.
53. S. Venugopalan and M. M. Becker, *Journal of Chemical Physics*, 1990, **93**, 3833-3836.
54. N. Koshizuka and S. Ushioda, *Physical Review B*, 1980, **22**, 5394-5399.
55. W. Y. Lee, H. J. Yun and J. W. Yoon, *Journal of Alloys and Compounds*, 2014, **583**, 320-324.
56. H. Kaneko, H. Ishihara, S. Taku, Y. Naganuma, N. Hasegawa and Y. Tamaura, *Journal of Materials Science*, 2008, **43**, 3153-3161.
57. F. J. Perez-Alonso, M. L. Granados, M. Ojeda, P. Terreros, S. Rojas, T. Herranz, J. L. G. Fierro, M. Gracia and J. R. Gancedo, *Chemistry of Materials*, 2005, **17**, 2329-2339.
58. C. A. Mccammon and D. C. Price, *Physics and Chemistry of Minerals*, 1985, **11**, 250-254.

59. F. J. Berry, S. Jobsen and S. L. Jones, *Hyperfine Interactions*, 1989, **46**, 613-618.
60. G. S. Li, R. L. Smith and H. Inomata, *Journal of the American Chemical Society*, 2001, **123**, 11091-11092.
61. R. C. Weast, *CRC handbook of chemistry and physics*, 1st student edition, CRC Press: Boca Raton, FL, 1988.
62. T. M. Onn, X. Y. Mao, C. Lin, C. Wang and R. J. Gorte, *Inorganics*, 2017, **5**, 69-80.
63. I. Moog, C. Prestipino, S. Figueroa, J. Majimel and A. Demourgues, *Journal of Physical Chemistry C*, 2014, **118**, 22746-22753.